

# UNIVERSITY OF



# MARYLAND

GPO PRICE \$ \_\_\_\_\_

CSFTI PRICE(S) \$ \_\_\_\_\_

Hard copy (HC) \_\_\_\_\_

Microfiche (MF) \_\_\_\_\_

ff 653 July 65

FACILITY FORM 602

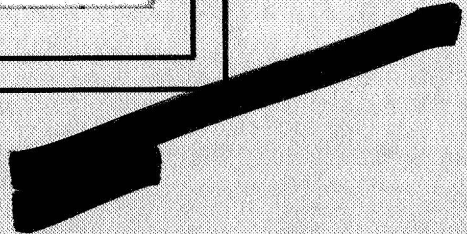
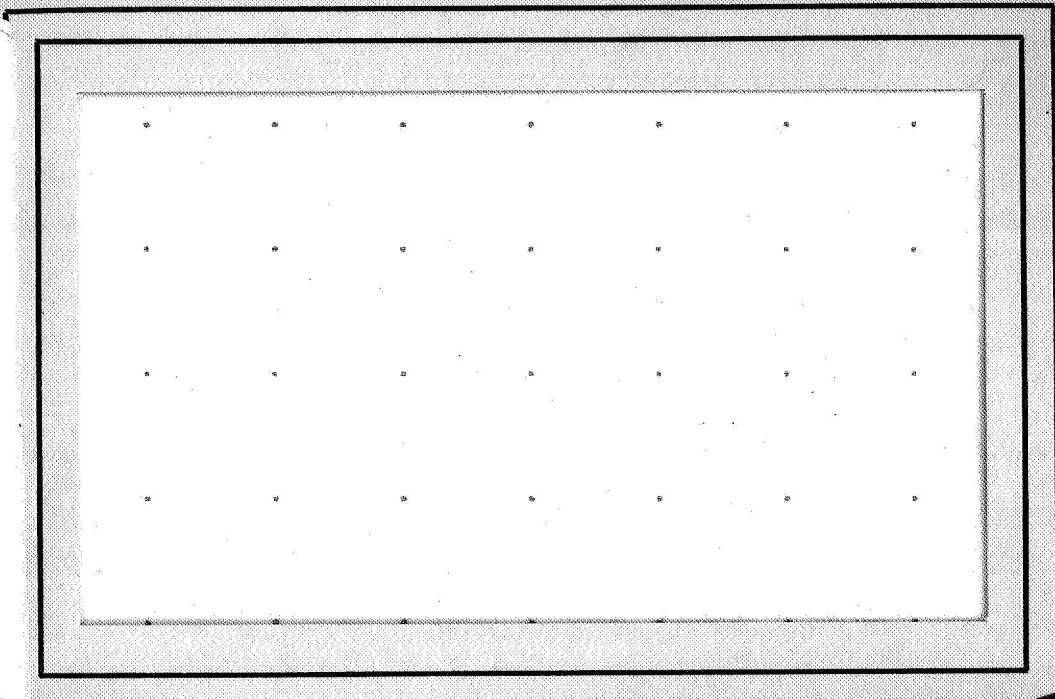
N 68-34264  
(ACCESSION NUMBER)

THRU \_\_\_\_\_  
(THRU)

30  
(CODE)  
(CATEGORY)

24  
(PAGES)

CR-8674  
(NASA CR OR TMX OR AD NUMBER)



THE INSTITUTE FOR FLUID DYNAMICS

*and*

APPLIED MATHEMATICS

Technical Note BN-482

November 1966

INSTABILITY OF THE EKMAN SPIRAL WITH  
APPLICATIONS TO THE PLANETARY BOUNDARY LAYERS

by

Alan J. Faller

and

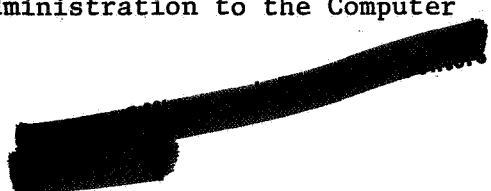
Robert Kaylor

University of Maryland  
College Park

This paper was presented at the IUGG-IUTAM Symposium on Boundary Layers and Turbulence Including Geophysical Applications, Sept. 19-24, Kyoto, Japan, and will appear in abridged form in The Physics of Fluids.

ACKNOWLEDGEMENT

The research reported in this paper was supported in part by the National Science Foundation under Grant NSF-GP-3443. The computer time was provided through Grant NsG-398 from the National Aeronautics and Space Administration to the Computer Science Center of the University of Maryland.



INSTABILITY OF THE EKMAN SPIRAL WITH APPLICATIONS  
TO THE PLANETARY BOUNDARY LAYERS

by

Alan J. Faller

and

Robert Kaylor

Institute for Fluid Dynamics and Applied Mathematics  
University of Maryland  
College Park

## ABSTRACT

The Ekman spiral boundary layer is a simple example of secondary flows where the velocity vector changes direction with distance from the boundary. The ideal Ekman spiral occurs in rotating systems near boundary surfaces perpendicular to the rotation axis when the flow is slow compared to the speed of rotation. Previous experimental and theoretical results on the shear-flow instability for a rigid boundary are briefly reviewed. New results are presented for the Ekman layer with a free boundary and for shear-flow instability in the presence of density stratification. The principle new results, obtained by means of numerical integrations of the equations of motion, are:

- 1) For the Ekman boundary layer caused by wind stress on a free water surface the critical Reynolds number is much less than for the case of flow over a smooth rigid boundary. Photographic examples of the instability due to wind stress obtained from laboratory experiments are also presented.
- 2) For the free-surface case the distortion of the basic boundary-layer flow by the finite-amplitude roll vortices is very great, to the extent that the modified mean flow may not be recognizable as an Ekman spiral.
- 3) With unstable density stratification either shear-flow instability or thermal convection may dominate according to the relative values of Rayleigh and Reynolds numbers.
- 4) With stable density stratification the shear-flow instability may be resonant with internal gravity-wave oscillations so that damping of the cellular circulations is minimized. This resonance may result in significant modification of the wave length and the orientation of the most unstable mode. Some of the implications of these results for the planetary boundary layers of the atmosphere and ocean are considered.

## 1. INTRODUCTION

The Ekman spiral describes the boundary layer in a rotating coordinate system where the flow is slow compared to the speed of rotation and the boundary is perpendicular to the rotation axis. It is a simple example of a class of boundary-layer flows in which the velocity changes direction as one moves normal to the boundary, and it is readily produced in rotating laboratory experiments. Figure 1 illustrates the normal component of flow for the Ekman boundary layer in comparison with that due to a rotating disc in a stationary fluid. Both boundary layers have similar instabilities when the Reynolds numbers for the laminar flows exceed their respective critical values. Experimental results for the rotating disc have been given by Gregory, Stuart and Walker<sup>1</sup> and for the Ekman boundary layer by Faller<sup>2</sup>, Faller and Kaylor<sup>3</sup>, and Tatro and Mollo-Christiensen<sup>4</sup>. Independent numerical studies of the instability of Ekman flow by the present authors<sup>5</sup> and by Lilly<sup>6</sup> are in essential agreement with the laboratory results and extend these results beyond what can be readily measured in the physical experiments.

In addition to direct application to many laminar rotating fluid systems, it has been suggested that the instabilities described here may be of significance in the turbulent planetary boundary layers of the atmosphere and the oceans<sup>7,8,9</sup>. There the average profiles of flow are similar to the Ekman spiral, and, indeed, it was in view of calculating the wind drift in the surface layers of the ocean that Ekman<sup>10</sup> first considered the solution for viscous boundary-layer flow in a rotating system. The essential basis of the suggested correspondence of the laminar results with the turbulent planetary boundary layers is this: When the effects of small-scale turbulence are

parameterized as an eddy viscosity it is found that the turbulent Reynolds number of the flow in a planetary boundary layer is generally such that it should be unstable to large-scale cellular motions<sup>8</sup>. While the limits within which this correspondence holds remains one of conjecture, there is abundant evidence of roll-vortex structure in the planetary boundary layers. In many cases these vortices may be due to organized thermal convection, but the possibility of cellular structure due to shear-flow instability deserves serious consideration and should not be excluded.

In this paper we will briefly review the essential results of previous work before proceeding to the more recent developments. Numerical and experimental results which complement this review will be given in other presentations by Drs. Lilly and Mollo-Christiensen, respectively. Our more recent work has concerned the following topics: 1) studies of the stability of Ekman flow due to wind stress on the free boundary of a liquid (the ocean surface case), 2) finite-amplitude numerical solutions with a free boundary, 3) numerical studies of Ekman shear flow in the presence of unstable density stratification, and 4) numerical studies of the effects of a stable density stratification on the instability of Ekman flow.

## 2. REVIEW

Figure 2 shows two examples of the distribution of a dye tracer in a rotating laboratory experiment, and illustrates some of the characteristics of the two modes of instability of the laminar Ekman boundary layer. In this experiment a vortex was generated by withdrawing water from the center of the tank (at the axis of rotation) and by reintroducing it at the rim. Away from the center of the tank the angular speed of flow was small compared

to the basic rotation rate of the system. The Ekman boundary layer at the bottom of the fluid (water) was approximately 0.5 cm thick compared to a total depth of 20 cm, and the radial transport of fluid took place entirely in this thin Ekman boundary layer. Crystals of potassium permanganate dye were dropped into the tank near the rim to illustrate the laminar flow and the two modes of instability. In Fig. 2b the laminar flow at the very bottom of the boundary layer is indicated by the streaks of dye spiraling inward at 45 degrees.

The vortex circulation was cyclonic, in the same sense as the tank rotation when viewed from above, and in Fig. 2 the free stream flow (above the boundary layer) is parallel to the circular lines, from right to left. The instability designated type 1 is shown by the small bands of dye oriented about 15 degrees to the left of the basic flow, and the instability designated type 2 is shown by the widely spaced bands oriented about 15 degrees to the right of the free stream flow. The circular lines are 20 cm apart in a tank of total radius 200 cm, hence for the experiment illustrated in Fig. 2a the type 1 bands had a spacing of  $L(1) = 2.33$  cm and the type 2 bands,  $L(2) = 6.25$  cm. In terms of the characteristic depth of the boundary layer  $D = (\nu/\Omega)^{1/2}$ , where  $\nu$  is the kinematic viscosity and  $\Omega$  is the basic rotation rate, the corresponding non-dimensional band spacings are  $L(1) = 11.1D$  and  $L(2) = 29.8D$ . In Fig. 2b the band spacings and angles are more variable, but the two modes are clearly distinguishable none the less. The bands of dye are indicative of roll-vortex circulations with horizontal axes, these circulations being superimposed upon the basic Ekman boundary-layer flow. They lead to alternating bands of convergence and divergence near the bottom of the boundary layer and hence to the dark and light bands, respectively.

It should be noted that the type 1 bands are nearly stationary. These are an example of inflectional instability similar to the stationary vortices observed and analyzed by Gregory, Stuart and Walker<sup>1</sup> for the rotating disc. On the other hand the long wave length type 2 vortices move rapidly and appear to be essentially different in character from the type 1 mode. Dr. Lilly, who's presentation follows, has shown that the type 2 vortices represent a new kind of instability in which the Coriolis forces play an essential destabilizing role as opposed to the type 1 vortices for which the Coriolis forces tend to stabilize the flow<sup>6</sup>. It has now been shown that the type 2 mode of instability occurs also for the flow due to a rotating disc when there is sufficient disturbance of the basic flow, and it has been inferred that the rapidly moving type 2 mode is most important for the transition to turbulence that is observed<sup>3</sup>.

Figure 3 gives schematically the results of our experiments on the incidence and the different regimes of these two modes. The abscissa is a Rossby number  $Ro$  which in this case measures the relative importance of curvature of the flow in the cylindrical tank<sup>2</sup>, and the ordinate is the Reynolds number  $Re$  at which the laminar flow was first observed to be unstable. For the Ekman boundary layer the Reynolds number is defined as  $Re \equiv \frac{V_g D}{\nu} = \frac{V_g}{(\Omega \nu)^{1/2}}$  where  $V_g$  is the geostrophic speed of flow (free-stream flow) above the boundary layer. The details of Fig. 3 are discussed elsewhere<sup>2,3</sup> but the major features of note are these: 1) The effects of curvature (as measured by  $Ro$ ) apparently have a strong influence upon the stability of the type 2 mode but a relatively small effect upon that of type 1; 2) The two intersecting lines define 4 stability regimes; and 3) For the ideal Ekman boundary layer ( $Ro = 0$ ) type 2 has a critical value of  $Re$



significantly less than for type 1. These facts have been confirmed by the experiments of Tatro and Mollo-Christiensen<sup>4</sup> who found the minimum critical Reynolds number to be  $Re_c(2) = 56$ , somewhat lower than the minimum value indicated by our data. Their experimental value was very close to the value  $Re_c = 55$  found by Lilly<sup>6</sup> and by us<sup>5</sup> in the two different numerical studies.

With respect to the effect of  $Ro$  upon the type 2 instability, there is some question about the significance of the sloping line as a true representation of the instability curve for the type 2 mode. Both sets of experimental observations<sup>3,4</sup> are in substantial agreement that such a sloping line represents the boundary between observable and non-observable vortices. However, because of the rapid radial motion of the type 2 mode it has been suggested<sup>5</sup> that the exponentially growing disturbance may not reach observable amplitude until it has moved radially inward to a value of  $Re$  significantly greater than the true critical value. In such a case the error in the estimation of  $Re_c$  would be a function of  $Ro$  and could lead to the apparent dependence of  $Re_c$  upon  $Ro$  that is indicated in Fig. 3.

### 3. EKMAN INSTABILITY WITH A FREE BOUNDARY

The Ekman spiral produced near the free surface of a rotating liquid by a constant tangential stress on the surface is the same in all essentials as that due to geostrophic flow over a rigid boundary. The spiral flow due to wind stress on a rotating body of water is illustrated in Fig. 11. In terms of non-dimensional length and velocity scales there is no difference in the shear of these two spiral boundary layers and all apparent differences of velocity can be accounted for by the reference velocity of the observer. However, even though the shear of the basic flow is the same in each case,

cellular or turbulent motions experience a rigid boundary in the one case and an essentially free boundary in the other. The equivalent definition of  $Re$  for the free surface case is  $Re \equiv \frac{v_0 D}{\nu} = \frac{v_0}{(\Omega \nu)^{1/2}}$  where  $v_0$  is the free surface speed for the undisturbed Ekman spiral.

Figure 4 shows the dependence of growth rate  $k$  upon the angle  $\epsilon$  (as defined below) and the wave number  $\alpha = \frac{2\pi D}{L}$  for the Ekman boundary layer due to a free surface stress at  $Re = 25$ . These results were obtained by a direct numerical integration of the Navier-Stokes equations by means of an initial value technique. Details of the formulation of this problem, the numerical procedures, and some results are given elsewhere for the rigid-boundary case<sup>5,9</sup>, and only a broad outline of the method is repeated here.

The equations to be integrated were, before conversion to finite-difference form,

$$\begin{aligned} \frac{\partial u}{\partial t} + Re \frac{\partial(\phi, u)}{\partial(y, z)} + 2 \frac{\partial \phi}{\partial z} &= \nabla^2 u \\ \frac{\partial \xi}{\partial t} + Re \frac{\partial(\phi, \xi)}{\partial(y, z)} - 2 \frac{\partial u}{\partial z} &= \nabla^2 \xi \end{aligned} \quad (1)$$

Here we have used right-handed Cartesian coordinates with  $z$  in the direction of the rotation vector. The coordinate scales have been made dimensionless with respect to the Ekman depth  $D$ , and the velocity components  $u, v, w$  have been made dimensionless with respect to  $v_0$ . The velocity is taken relative to the rotating coordinate system, and the resultant Coriolis accelerations are the third terms on the left of eqs. (1). The  $x$  direction has been taken at the angle  $\epsilon$  to the left of the free-surface flow and is the direction of the axes of the cellular motions. Since the basic flow and the cells are independent of  $x$ , due to the continuity equation the velocity components in the  $y-z$  plane can be represented by a stream function defined by

$w = \partial\phi/\partial y$  and  $v = -\partial\phi/\partial z$ . Accordingly,  $\xi$  is the component of vorticity in the  $x$  direction. The angle  $\epsilon$  and the wave-length  $L$  are treated as parameters to be varied from one numerical experiment to another to determine the values of  $\epsilon$  and  $L$  which result in the maximum instability at some value of  $Re$ .

The boundary conditions for the free-surface problem are:

$$\begin{aligned} \text{at } z = 0 & : \quad \partial u/\partial z = 2^{\frac{1}{2}} \cos(\pi/4 - \epsilon) , \quad \partial v/\partial z = 2^{\frac{1}{2}} \sin(\pi/4 - \epsilon) \\ \text{at } z = -\infty & : \quad \partial u/\partial z = 0 , \quad \partial v/\partial z = 0 . \end{aligned}$$

These conditions lead to the solution of eqs. (1):

$$\begin{aligned} u &= e^z \cos(z - \epsilon) \\ v &= e^z \sin(z - \epsilon) , \end{aligned} \tag{2}$$

and it is the stability of eqs. (2) that is under consideration.

The initial conditions for the numerical integrations were eqs. (2) plus a small perturbation introduced into the finite-difference analogue of eqs. (1). Growth rates  $k$  were determined from the rate of change of amplitude of the dominant unstable mode after the initial perturbations were no longer important but before the unstable cellular motions had reached large enough amplitude to significantly alter the basic flow.

From Fig. 4 it appears that at  $Re = 25$  the most unstable mode occurred at approximately  $\epsilon = 4 \pm 2$  degrees and  $\alpha = 0.42 \pm .05$ . This value of  $\alpha$  corresponds to  $L = 15.0 \pm 2.0D$ . From similar data we have extrapolated to  $k = 0$  and find the preliminary estimate  $Re_c = 12 \pm 3$  as the minimum critical Reynold number.

Figure 5 is an example of the form of the cellular motions for the free surface case. Although this example is for finite-amplitude conditions where the mean flow has been somewhat changed by the non-linear interactions,

nevertheless the general cellular structure is indicated. Of particular note in Fig. 5 is the fact that the most unstable mode does not consist of a series of alternating cells which damp in intensity with depth. Rather, the cells extend without significant change of phase to the bottom of the fluid layer, as is indicated by the vertical 0 lines separating positive and negative values of stream function. The cells in Figure 5 that are indicated by dashed lines at approximately  $z = -10$  do not contradict the above statement since they are a result of the non-linear interactions and do not appear for the small-amplitude, exponentially growing mode of instability.

We have made a preliminary attempt to obtain experimental confirmation of the numerical results discussed above. Figure 6 shows bands of dye which illustrate wind-driven vortices near the free surface of a rotating tank of water. Wind stress was generated by rapidly rotating a light-weight aluminum frame with twelve radial arms close to the water surface (see Fig. 7.). Although surface waves also were generated, these did not seem to interact with the Ekman boundary layer to a significant extent. Crystals of Acid Fuchsin, a red dye, were sprinkled onto the surface to indicate the circulation. At first they showed the direction of flow at the free surface, then the dye became organized into bands by the roll vortices, and finally the dye became mixed and diffused throughout a deep layer and no longer indicated the vortex motions.

Unfortunately, a contaminating surface film had a strong influence upon the wind-driven circulation. Figure 8 illustrates how the water in the central portion of the tank was swept clean of the contaminating film by the radial motion in the surface layer. In the film-covered region toward the rim of the tank the surface flow  $v_0$  was constrained to be purely tangential. If the surface flow had had a radial component the film would have compressed

(or dilated) until this component of surface flow vanished. In the equilibrium state the total stress  $\tau_t$  was the sum of the wind stress  $\tau_w$  and the pressure effect due to the compressed film  $\tau_p$ . In the film-free region the wind stress was the only surface force. The Ekman spirals with surface flow 45 degrees to the right of the total stress are shown in Fig. 8 for both regions.

In Fig. 6 banded structures are shown for both the filmed and the film-free regions. In the latter case (Figure 6b) a sequence of three photos at intervals of 6 secs. shows the development of the banded structure from an initially unbanded pattern of dye. By comparison of the band orientations with the Ekman spirals in Fig. 8 and with the surface flows indicated by the dye streaks (Fig. 6b) it appears that in both cases the bands were oriented about 10-15 degrees to the right of the surface flow. This result disagrees with our numerical results which indicated that the angle of maximum instability was approximately 4 degrees to the left of the surface flow. However, there are several ways in which the experiments do not conform to the idealized model used for the numerical integrations. First, the effect of a surface film (or even surface tension in the absence of a contaminating film) may alter the most unstable mode. Second, the rate of rotation of the tank was kept low to maintain an essentially flat water surface, and as a result the boundary layer may have differed considerably from the ideal Ekman solution. Third, although the surface gravity waves appeared to have little influence, some small distortion of the boundary-layer flow probably was introduced by interaction with the waves. Finally, the vortices indicated by the bands of dye were finite-amplitude circulations at values of  $Re$  in the range 50-100. Thus the experiments have demonstrated an instability of the

wind-driven surface boundary layer, but a detailed comparison of theory and experiment will require better correspondence between the experimental and the numerical studies.

#### 4. FINITE-AMPLITUDE RESULTS FOR INSTABILITY WITH A FREE-SURFACE

Figures 9 and 10 illustrate the results of a numerical computation carried out until a steady-state finite-amplitude solution was attained. The computation was performed for  $Re = 600$  and  $\epsilon = 30$  degrees. The horizontal wave lengths  $L = 24, 12, 8,$  and  $6D$  were permitted in the computation to allow non-linear interactions of these modes, as opposed to some other cases where only the longest wave permitted by the grid was allowed to occur. Angle  $\epsilon = 30$  degrees corresponds to vortices oriented 30 degrees to the left of the surface flow or 15 degrees to the right of the wind stress. The depth of the fluid was rather shallow and undoubtedly this restricted the vertical development of the cells. This limitation and the specific values of  $\epsilon$  and  $L$  that were used must have affected the specific detailed results but do not seem to have been crucial for the general results that are described below.

As may be inferred from Fig. 9, the 4 permitted horizontal modes all achieved significant amplitude and became locked in phase to produce a single intense cell which extended to the bottom of the fluid. By comparison of the total stream function with the perturbation stream function it is clear that the velocities of the cellular motions were comparable with the mean flow. Figure 9 shows that departures of  $u$  from the horizontally averaged flow attained values greater than 50% of  $v_0$ . Moreover, since the original shear

flow was essentially confined above the depth  $z = -2$  we see that the cellular motions that arose from the instability penetrated well beneath the original boundary layer.

Figure 10 illustrates the modification of the original spiral by the strong cellular motions through the vertical exchange of momentum. In comparing the original Ekman spiral with the mean flow after complete development of the cells we find that 2 principal modifications of the original flow have taken place: 1) the free-surface flow has been reduced to  $0.61 v_0$ , and the angle with respect to the wind has been reduced from 45 degrees to 8 degrees. 2) The steady-state transport to the right of the wind stress became distributed throughout nearly the entire depth of the fluid layer.

We have not determined that the specific conditions of the experiment described above are the optimum in any sense, and it may be that a different combination of  $L$  and  $\epsilon$  would occur naturally in a physical experiment. More numerical and experimental studies will be required to clarify this question. In the meantime it appears that significantly large modifications of the basic flow can result from these instabilities, to the extent that it may not be recognizable as an Ekman spiral.

## 5. SHEAR-FLOW INSTABILITY WITH UNSTABLE DENSITY STRATIFICATION

One of the most important factors that must be considered in the planetary boundary layers of the atmosphere and ocean is density stratification. With an unstable thermal gradient one might suppose that thermal convection would dominate over the shear-flow instability, and with stable stratification one might expect that the shear-flow instability might be rapidly damped.

To incorporate stratification into our numerical model we have added the heat energy transfer equation to the equations of motion and continuity and have introduced the Boussinesque approximation. The following equations apply to geostrophic flow over a rigid boundary:

$$\begin{aligned} \frac{\partial u}{\partial t} + \text{Re} \frac{\partial(\phi, u)}{\partial(y, z)} + 2 \frac{\partial \phi}{\partial z} &= -2 \sin \epsilon + \nabla^2 u \\ \frac{\partial \xi}{\partial t} + \text{Re} \frac{\partial(\phi, \xi)}{\partial(y, z)} - 2 \frac{\partial u}{\partial z} &= \frac{\text{RaPD}^3}{\text{ReH}^3} \frac{\partial \alpha}{\partial y} + \nabla^2 \xi \\ \frac{\partial \alpha}{\partial t} + \text{Re} \frac{\partial(\phi, \alpha)}{\partial(y, z)} &= P \nabla^2 \alpha, \quad \xi = \nabla^2 \phi \end{aligned} \quad (3)$$

In eqs. (3) Ra is a Rayleigh number, P is the Prandtl number, H is the depth of the fluid, and  $\alpha'$  is the specific volume. For this study  $\text{Ra} = -\frac{g \Delta \alpha' H^3}{\alpha'_0 \kappa \nu}$  where  $\alpha'_0$  is the initial average value of  $\alpha'$ ,  $\Delta \alpha' = \alpha'_u - \alpha'_l$  is the difference in  $\alpha'$  between the upper and lower boundaries of the fluid, and we have taken initially a linear gradient of  $\alpha'$  given by

$$\alpha'_0 = \alpha'_0 + \Delta \alpha' \left( \frac{zD}{H} - \frac{1}{2} \right) .$$

The dimensionless value of the departure of the specific volume from the initial linear gradient is  $\alpha = \frac{\alpha' - \alpha'_0}{\Delta \alpha'}$ . We consider first the case of a gravitationally unstable density stratification which, from the above definitions, corresponds to negative  $\Delta \alpha'$  and positive Ra.

In Fig. 11 we have summarized the interaction of convective cells with the shear flow in an Ekman layer at low values of Re. The shear flow was essentially confined to the layer below  $z = 2$ , but the thermal cells could extend throughout the entire depth of the fluid, in this case to  $H = 8D$ . The nearly-vertical curves in Fig. 11 show the vertical variation of the relative amplitude of the stream function  $\phi$  in the thermal cells at the constant



value  $Ra = 10^5$  and for the three values  $Re = 0, 50, \text{ and } 100$ . The nearly-horizontal curves indicate the height of the maximum in stream function,  $\phi_{\max}$ , as a function of  $Re$  for the three wave lengths  $L = 6, 12 \text{ and } 24D$ . For increasing  $Re$  and for each value of  $L$  it appears that the height of  $\phi_{\max}$  increases gradually and approaches a limiting height at about  $z = 5.1$  compared to the height  $z = 4.0$  at  $Re = 0$ . The dashed curves indicate the growth rate  $k$  for each value of  $L$  as a function of  $Re$ . These curves show a decrease of  $k$  with increasing  $Re$ . The overall interpretation is that above  $Re \approx 50$  the convective cells are in effect cut off by the shear flow and are confined to the fluid region above the Ekman layer. With the reduction in the vertical extent of the cells there is an accompanying decrease in their growth rate due to the dependence of  $Ra$  upon the depth of convection.

For still larger  $Re$  we must consider the possibility of competition between the thermal and the shear-flow instabilities. Fig. 12 shows patterns of stream function at two different times during a computation for  $Re = 300$ ,  $Ra = 10^5$  and  $\epsilon = 14$  degrees. For this experiment the initial conditions were thermal cells that extended through the entire depth of the fluid. At  $Re = 300$  these were rapidly truncated at the bottom by the shear flow. In Fig. 12a the beginning of a shear-flow instability is indicated by the low level cells, but the thermal cells at higher levels still dominated the circulation. However, for these values of  $Re$  and  $Ra$  the rate of growth of the shear-flow instability was greater than for the truncated thermal convection, and Fig. 12b shows the conditions at a later time when the shear flow instability began to dominate. For these conditions the growth rates of the thermal and the shear-flow cells determined independently were, respectively  $k_t = 4.8$  and  $k_s = 11.1$ .

An interesting feature of this computation was the large oscillation of the energy of the flow as the transition from thermal to shear-flow cells progressed. At this angle ( $\epsilon = 14$  degrees) the shear-flow cells were nearly stationary, but the thermal cells at the same angle were imbedded in an upper level flow which had a significant component normal to the axes of the cells, to the left in Figure 12. As a result, when the two cellular structures were of approximately equal magnitude there were large fluctuations of the pattern and of the perturbation energy as the upper and lower cells came into and out of phase. When in phase the cells merged and extended throughout the entire layer. These results are of a preliminary nature and a more comprehensive survey of parameters including studies for finite-amplitude circulations is needed. Nevertheless, many interesting aspects of the interaction of shear-flow instabilities and thermal convective instabilities have already appeared.

#### 6. EKMAN INSTABILITY WITH A STABLE DENSITY STRATIFICATION

It is not obvious that a stable density stratification in a planetary boundary layer will always damp the large-scale shear-flow instability with which we are concerned, for two reasons. First, while on the one hand we expect that for a given  $Re$  stable stratification will tend to damp cellular motions, on the other hand the small-scale turbulence is also damped. Accordingly, one should expect an increase in the turbulent Reynolds number,  $Re_t = V_g / (\Omega \nu_t)^{1/2}$ , where  $\nu_t$  is the turbulent or eddy viscosity that is used to parameterize the small-scale turbulence. Because of the latter effect we might expect an increase in the tendency for large-scale instability of the boundary layer. Second, there is the possibility that the moving cells will travel with the speed of internal gravity waves and thus provide a resonance

between the gravity mode and the shear-flow instability. We have begun a study of this latter possibility using numerical solutions of Eqs. (3) with negative values of  $Ra$ , stable stratification.

An upper bound for the frequency of internal gravity waves in an otherwise stationary fluid is given by the Brunt-Vaisala frequency<sup>11</sup>. In effect, this is the natural frequency of oscillation of a parcel of fluid displaced vertically from its equilibrium position in a stable stratification and allowed to oscillate without exchange of mass, heat, or momentum with its environmental fluid. In terms of the parameters already defined the Brunt-Vaisala frequency is given by  $\omega^* = (RaD^4/PH^4)^{1/2}$  where  $\omega^*$  has been made dimensionless with respect to  $\Omega$ . The corresponding upper bound on the speed of an internal wave of given wave length  $L/D$  is  $c = \pm \omega^*L/2\pi DRe$ .

Since the main body of the fluid layer under consideration moves in the  $y$  direction with a speed  $\sin \epsilon$ , the interval of speeds in which internal gravity waves can exist is given by  $c_g = \sin \epsilon \pm \omega^*L/2\pi DRe$ . Consequently, resonance between the shear flow instability and one or more of the many internal wave modes can occur only when the speed of the unstable mode lies within the range of speeds cited above. Of course, the speed of an unstable mode depends upon  $L/D$  and  $\epsilon$  as well as the parameters  $Re$ ,  $Ra$ , and  $H/D$ . In addition the possible internal gravity modes will be complicated by the boundary conditions and the shear of the basic flow, and several different internal modes may be excited simultaneously.

We have not yet attempted to analyze these complications in detail, but we present an example of what appears to be resonance. Figure 13 illustrates the growth rate as a function of  $\epsilon$  for the conditions  $Re = 600$ ,  $L/D = 24$ ,  $H/D = 12$ , and for

the two values  $Ra = 0$  and  $Ra = -2.4 \times 10^7$ . Plotted beneath the curves of growth rate are the phase speeds. The curve of  $k$  vs.  $\epsilon$  for  $Ra = 0$  shows a single maximum at approximately  $\epsilon = 20$ , while for  $Ra = -2.4 \times 10^7$  a second maximum occurs at about  $\epsilon = -20$ . At the latter angle the phase speed was about  $c_r = +0.55$ . From the value of  $Ra$ ,  $P$ , and  $H/D$  that were used, the Brunt-Vailsala frequency was  $\omega^* = 33$  so that for  $\epsilon = -20$  and  $L/D = 24$  the range of speeds for resonance was  $+0.552 > c_g > +0.132$ . However, for  $\epsilon = 0$  the range of speeds for resonance was  $+0.210 > c_g > -0.210$  compared to the observed speed of the decaying mode  $c_r = +0.28$ . These results indicate that resonance with internal gravity waves provides a mechanism for vortices at other angles than that which is most unstable at  $Ra = 0$ . In fact, there is the distinct possibility of the joint occurrence of two or more unstable modes at different angles in patterns similar to those of Fig. 2 but for a different reason.

The above study does not constitute definitive work on the mode that is most likely to appear even for the idealized model and the specified conditions that we have considered. With specific values of  $Ra$ ,  $Re$ ,  $P$ , and  $H/D$  it is still necessary to cover a wide range of values of  $L/D$  and  $\epsilon$  to determine that combination which gives the greatest growth rate. Further beyond lies the realm of finite-amplitude studies and extension of the number of independent parameters in order to more closely approximate the complicated conditions that prevail in the atmosphere and the oceans.

## 7. CONCLUSIONS

We have presented several new results concerning the instability of laminar Ekman boundary layers and have intimated the relevance of these results to the planetary boundary layers of the atmosphere and the oceans. The principal new results are summarized here:

1) We have shown examples <sup>of</sup> laboratory experiments which illustrate the instability due to wind stress on the surface of a rotating liquid. The corresponding numerical studies indicate that the minimum critical Reynolds number for this instability is much lower, approximately  $Re_c = 12$ , than for the case of geostrophic flow over a rigid boundary,  $Re_c = 55$ .

2) Finite-amplitude numerical studies for the free surface case indicate that the unstable cellular motions grow to much greater amplitude than for the rigid boundary case, penetrate to much greater depths into the fluid, and alter the average boundary-layer flow to the extent that its original Ekman spiral structure may disappear. These results have serious implications for the study of the planetary boundary layer in the oceans if, indeed, we can assume that the cellular circulations found there are caused by this mechanism. While there is abundant evidence of cellular circulations in the ocean <sup>12,13,14,15,16</sup> there is considerable disagreement upon the nature and origin of the observed cells that has given rise to other suggested mechanisms <sup>17</sup>.

3) The numerical studies for unstable thermal stratification indicate interesting interactions of the shear flow with thermal convection. First, the shear flow in the Ekman layer may simply cut off the convective cells so that they are confined to the region above the layer of shear flow. Second, either the shear-flow instability or thermal convection may dominate depending upon the relative magnitudes of  $Re$ ,  $Ra$ , and other parameters. Third, since the cells due to shear flow and those due to thermal convection move at different speeds there are interesting interactions which result in complicated transient patterns of flow. All of the above results depend, of course, upon the relative magnitudes of Rayleigh and Reynolds numbers. In the real geophysical situation it may be

expected that other complications, e.g. the diurnal transients or the requirement of heat transport, may lead to exceedingly complex interactions.

4) The influence of stable stratification upon the Ekman instability may not be a simple damping effect. In particular, our numerical results have demonstrated the possibility of resonance with internal gravity oscillations, this resonance being a function of the angle of the unstable vortices with respect to the geostrophic wind. These results suggest that roll vortices in the planetary boundary layer of the atmosphere may occur under conditions of stable density stratification and may occur at large angles with respect to the geostrophic wind.

#### ACKNOWLEDGEMENT

The research reported in this paper was supported in part by the National Science Foundation under Grant NSF-GP-3443. The computer time was provided through Grant NsG-398 from the National Aeronautics and Space Administration to the Computer Science Center of the University of Maryland.

## REFERENCES

- <sup>1</sup>N. Gregory, J.T. Stuart and W.S. Walker, Phil. Trans. Roy. Soc. London, A, 248, 155 (1955).
- <sup>2</sup>A.J. Faller, J. Fluid Mech., 15, 560 (1963).
- <sup>3</sup>A.J. Faller and R.E. Kaylor, The Dynamics of Fluids and Plasmas (Academic Press, New York, 1966).
- <sup>4</sup>P.R. Tatro and E. Mollo-Christiensen, J. Fluid Mech., 19 (Accepted for publication)(1967).
- <sup>5</sup>A.J. Faller and R.E. Kaylor, J. Atmos. Sci., 23, 466 (1966).
- <sup>6</sup>D.K. Lilly, J. Atmos. Sci., 23, 481 (1966).
- <sup>7</sup>A.J. Faller, Proc. 2nd Tech. Conf. on Hurricanes, Amer. Meteor. Soc., 307 (1961).
- <sup>8</sup>A.J. Faller, J. Atmos. Sci., 22, 176 (1965).
- <sup>9</sup>A.J. Faller, Proc. 5th U.S. National Congress of Appl. Mech., 651 (1966).
- <sup>10</sup>V.W. Ekman, Arkiv. Math. Astron, Physik, 2, 1 (1905).
- <sup>11</sup>D. Brunt, Physical and Dynamical Meteorology, 2nd Ed (Cambridge University Press, London, 1939).
- <sup>12</sup>I. Langmuir, Science, 87, 119 (1938).
- <sup>13</sup>A.H. Woodcock, J. Mar. Res., 5, 196 (1944).
- <sup>14</sup>A.H. Woodcock, J. Mar. Res., 9, 77 (1950).
- <sup>15</sup>W.H. Sutcliffe, E.R. Baylor and D.W. Mensel, Deep-sea Res., 10, 233 (1963).
- <sup>16</sup>A.J. Faller and W.H. Woodcock, J. Mar. Res., 22, 22 (1964).
- <sup>17</sup>P. Welander, Tellus, 15, 1 (1963).

## CAPTIONS

Fig. 1. Boundary-layer components of flow normal to the direction at angle  $\epsilon$  with the tangential direction. The principal inflection point in each profile is indicated by the curves I. The Ekman and rotating-disc boundary layers have similar instabilities.

Fig. 2. Examples of the simultaneous occurrence of the type 1 and type 2 modes of instability of the laminar Ekman boundary layer. a) The type 1 mode appears principally in the upper left and the type 2 mode in the center of the photograph. The interference pattern of the two modes is clearly seen in the upper left. b) The laminar region where streaks of potassium permanganate dye at the bottom of the Ekman layer spiral inward at 45 degrees appears in the upper right of the photograph. The pattern in the center is dominated by the type 2 mode of instability but the small bands of the type 1 mode are clearly visible. In both a) and b) transition to turbulence follows rapidly after the appearance of the type 2 instability, i.e. at smaller radius. These experiments were performed in a large rotating tank formerly in use at the Woods Hole Oceanographic Institution.

Fig. 3. The transition diagram for the type 1 and type 2 modes of instability. The dashed line and the solid line represent the observed values of  $Re$  vs  $Ro$  for instability of the type 1 and the type 2 modes, respectively. Since  $Ro$  measures the effect of curvature of the flow in the cylindrical tank, the extrapolated values at  $Ro = 0$  are the estimated critical Reynolds numbers for linear Ekman flow.



Fig. 4. A growth rate diagram for Ekman instability with a free boundary. The amplification rate  $k$  is given as a function of wave number  $\alpha$  and angle  $\epsilon$ (degrees) for  $Re = 25$ .

Fig. 5. Patterns of flow for Ekman instability with a free surface as determined by a numerical integration of the equations of motion. Conditions:  $Re = 500$ ,  $\epsilon = 20$  degrees,  $L = 12D$ ,  $H = 36D$ . The perturbation stream function is the departure from the horizontal average of the total stream function. The perturbation  $u$  is the departure from the horizontal average of  $u$ .

Fig. 6. The instability of wind-driven Ekman flow as indicated by bands of Acid Fuchsin dye near the free surface of the water. a) Bands of dye in the film-covered region. b) A sequence at intervals of 6 secs to show the development of the dye bands in the film-free region of the experiment. The different orientations of the bands, i.e. nearly tangential in (a) and nearly radial in (b), are due to the effect of the surface film on the orientation of the Ekman spiral (see Fig. 8). The boundary of the film-free region may be seen near the top of each photograph in (b).

Fig. 7. The rotating tank at the University of Maryland. Wind stress was provided by the rotating aluminum frame suspended approximately 3 cm above the water surface.

Fig. 8. The effect of a compressed surface film on the orientation of the wind-driven Ekman spiral. In the film-covered region the surface flow  $v_0$  was constrained to be purely tangential.

Fig. 9. Patterns of flow due to Ekman instability with a free surface.

Conditions of the numerical experiment:  $Re = 600$  ,  $\epsilon = 30$  degrees ,  
 $L = 24D$  ,  $H = 9D$  . The small difference between the total stream function and the perturbation stream function indicates dominance of the cellular motions over the mean flow. (Also see Fig. 10).

Fig. 10. Modification of the original Ekman spiral by the finite-amplitude cellular circulations shown in Fig. 9.  $W$  indicates the direction of the wind stress, and the dashed curve indicates the modified mean flow after interaction of the cells with the original Ekman spiral (solid curve). Numbers beside each curve indicate the non-dimensional depth.

Fig. 11. Modifications of thermal convection by the Ekman spiral shear flow at small  $Re$  for the three wave lengths  $L = 6D$  ,  $12D$  , and  $24D$  . The left-hand vertical scale is the grid height  $m$  where  $z = 0.2 m$  , and the right-hand vertical scale is the growth rate of amplitude of the thermal cells (dashed lines). The solid "horizontal" curve indicates the height of the center of the convective cells as a function of Reynolds number.

Fig. 12. The competition between thermal-convective and shear-flow instabilities. a) At this time and earlier in the numerical integration the upper level thermal cells dominated the pattern of stream function. b) At this later time the faster growing cells due to shear-flow instability began to dominate the pattern. Conditions of the numerical experiment:  $Re = 300$  ,  $Ra = 10^5$  ,  $\epsilon = 14$  degrees ,  $L = 24D$  ,  $H = 8D$  . Note that although the field of the numerical grid allowed development of the longer wave length  $L = 24D$  , the most unstable wave length was  $L = 12D$  .

Fig. 13. The growth rate  $k$  and phase speed  $c_r$  for Ekman instability with a stable density stratification. The secondary maximum at  $\epsilon = -20$  degrees for  $Ra = -2 \times 10^7$  corresponds to resonance with the internal gravity wave traveling at the same value of  $c_r$ .

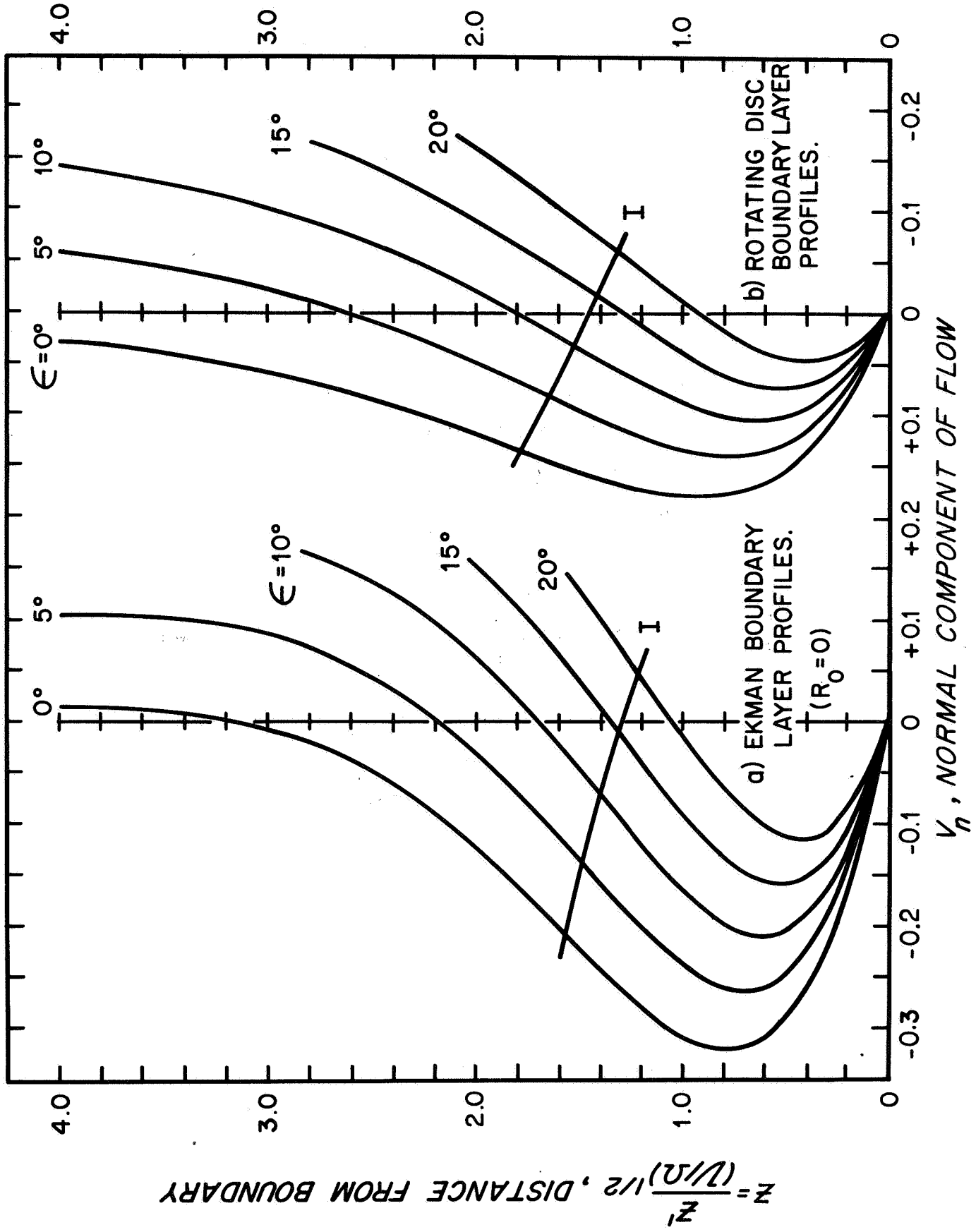


Figure 1

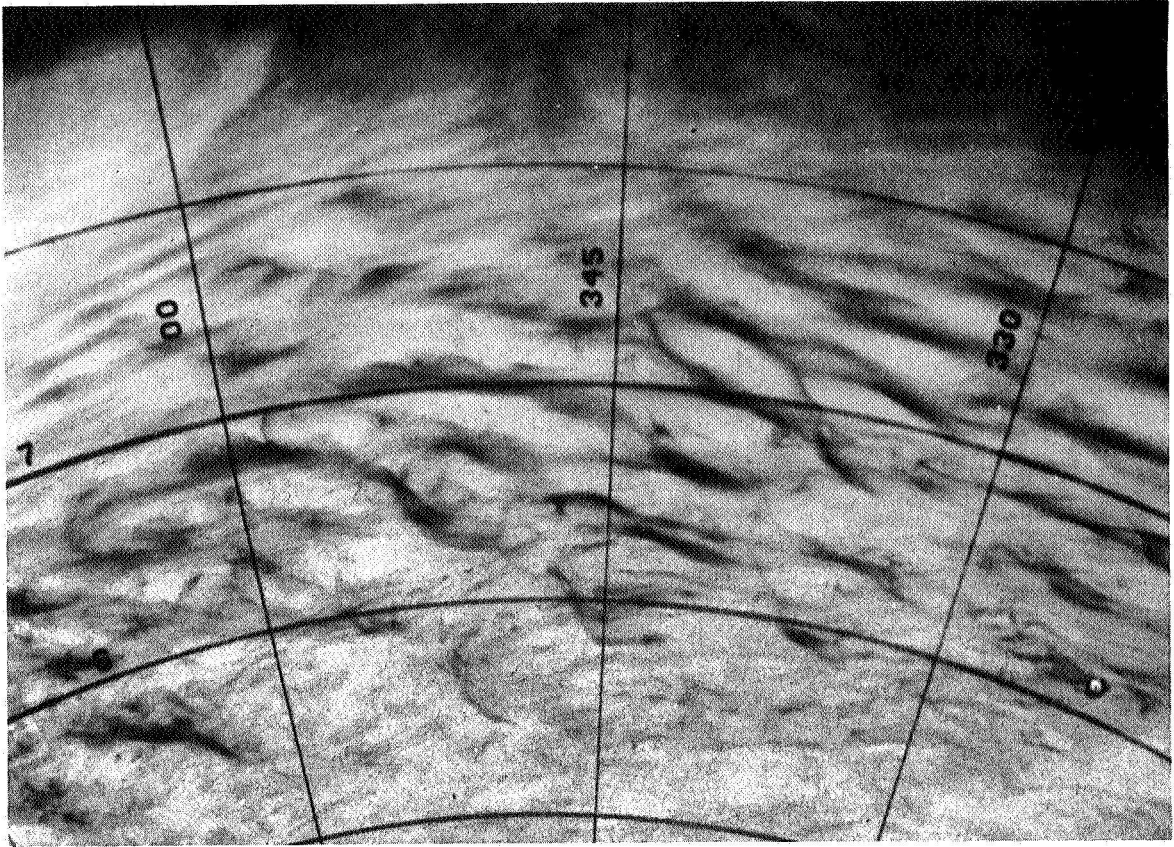


Figure 2a

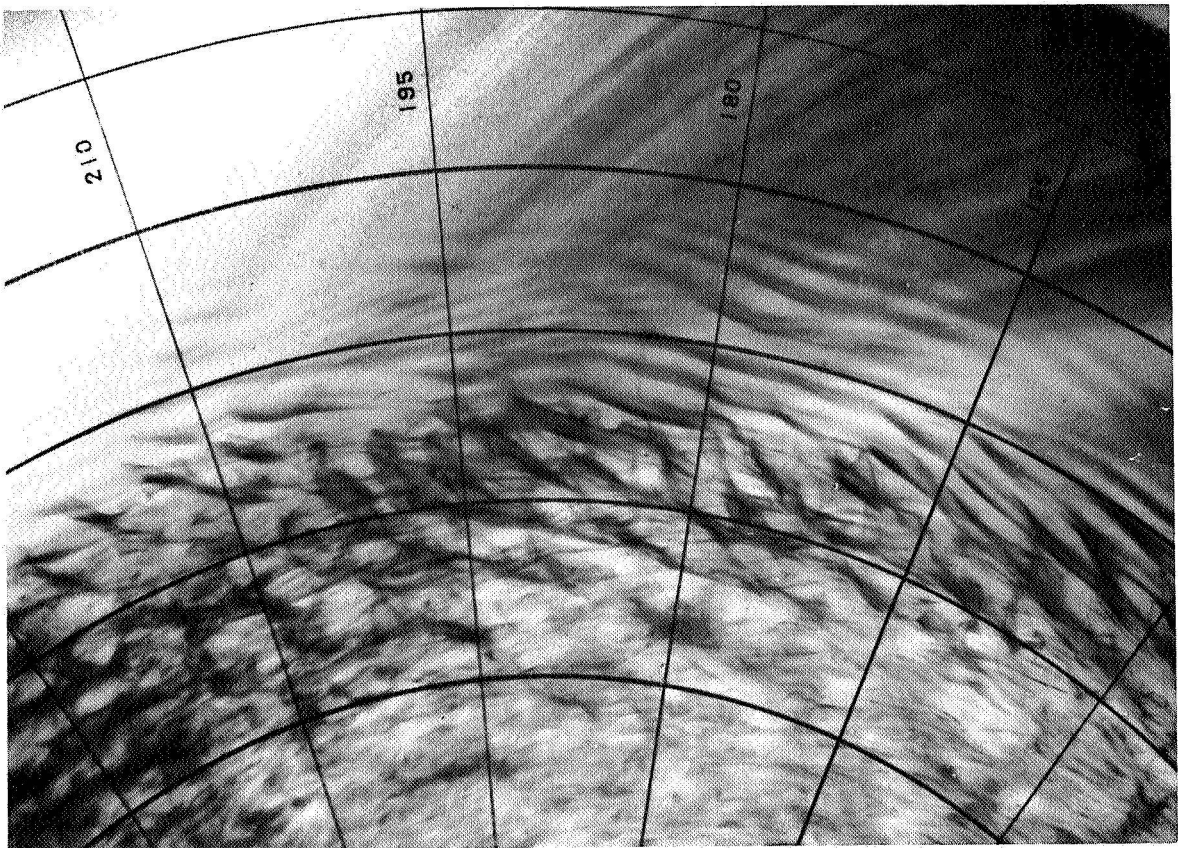
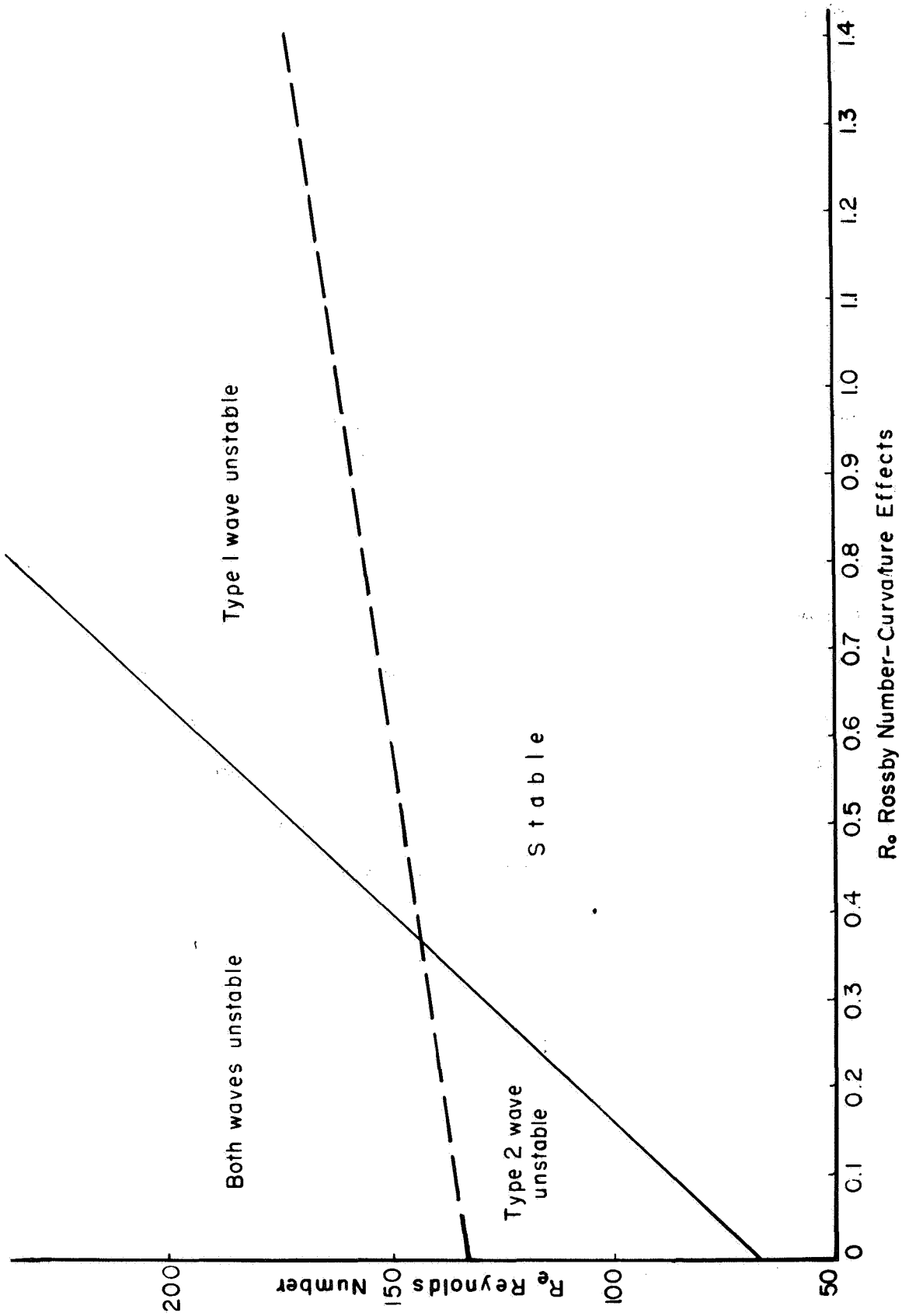


Figure 2b



**Figure 3**

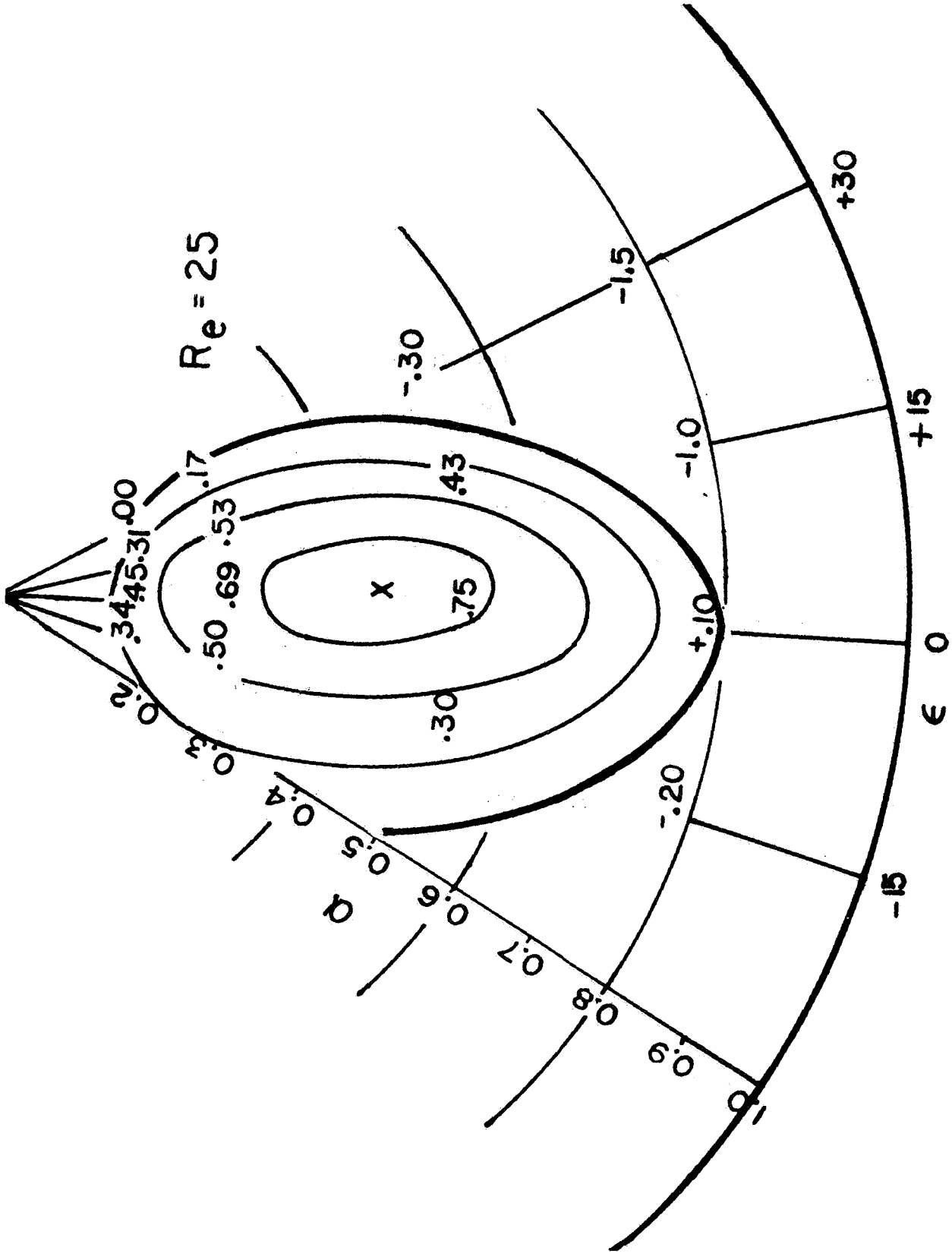


Figure 4

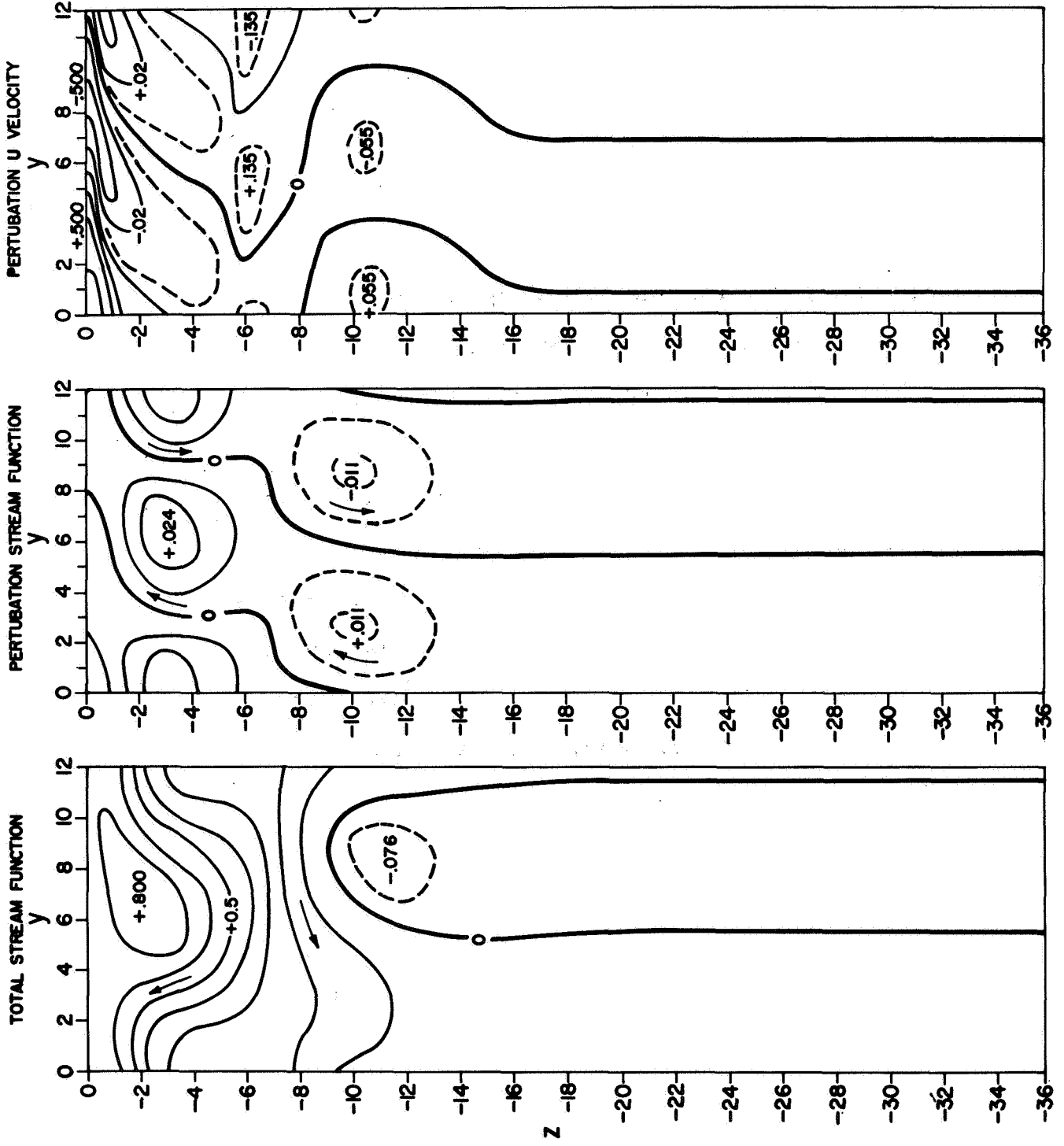


Figure 5



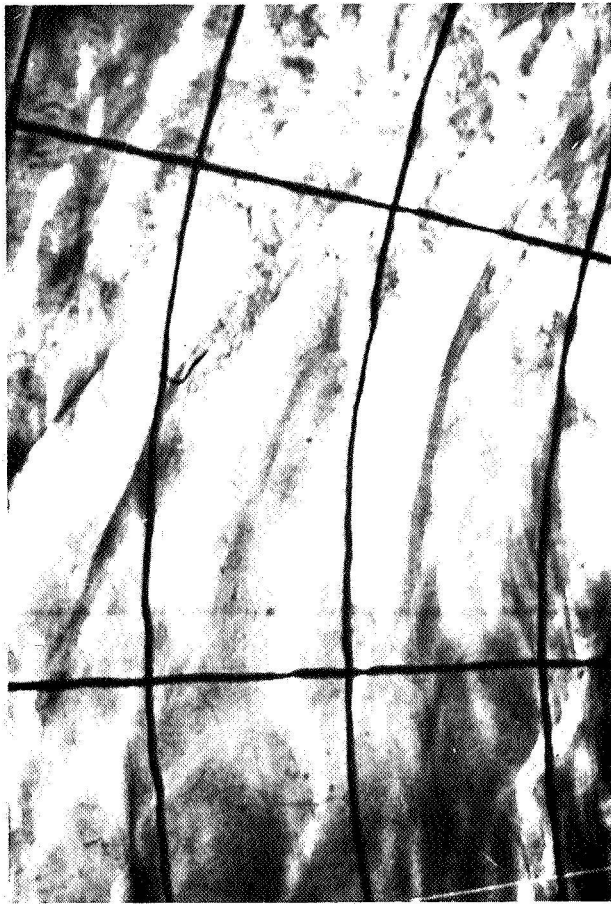


Figure 6a

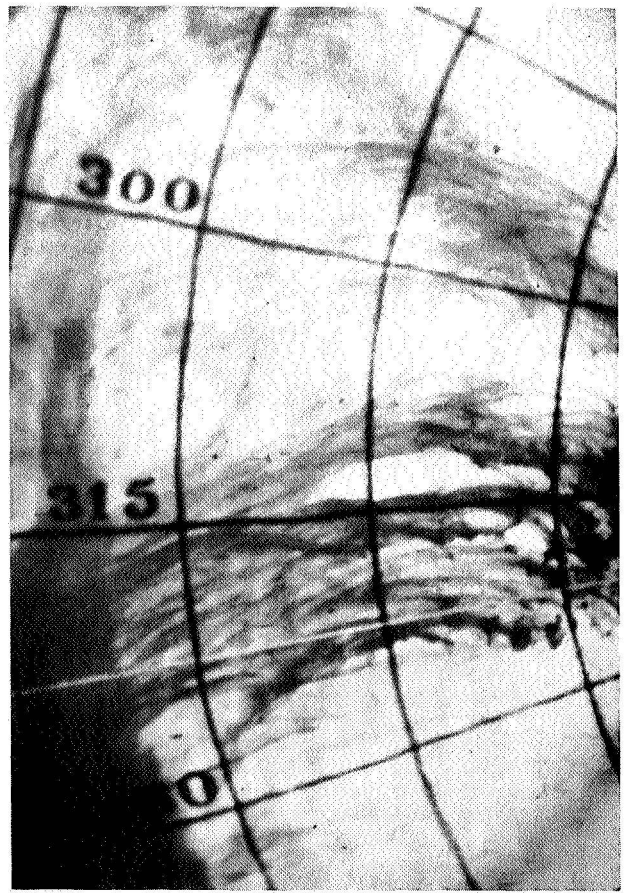


Figure 6b2

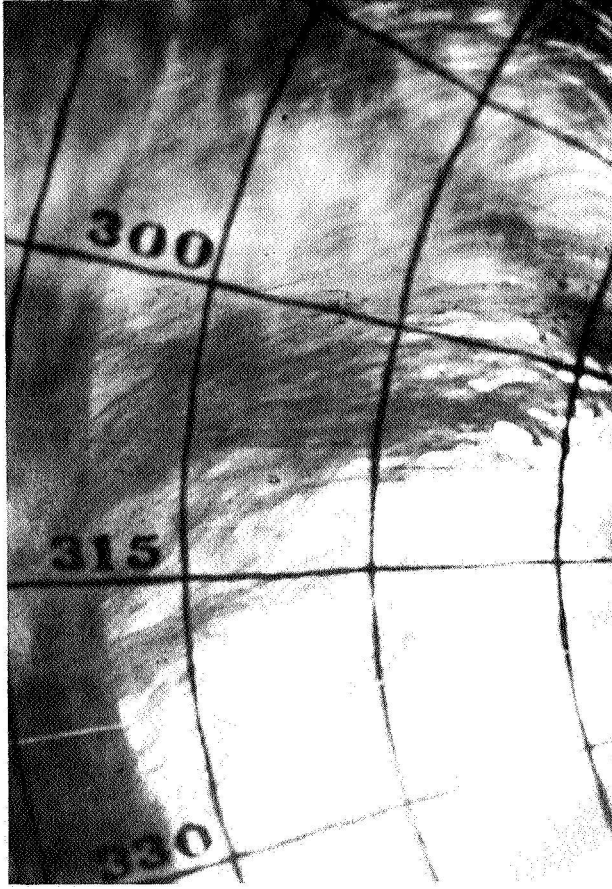


Figure 6b1

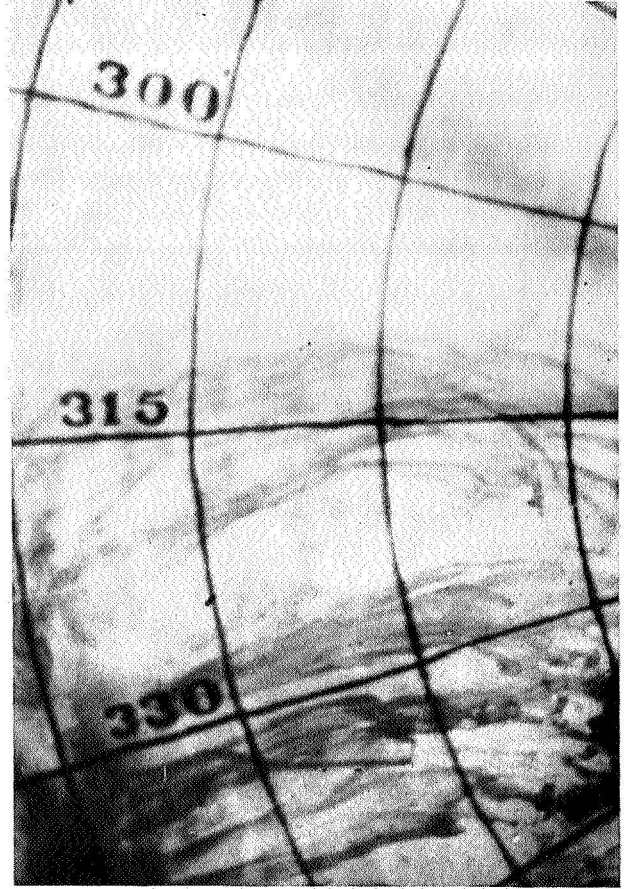


Figure 6b3

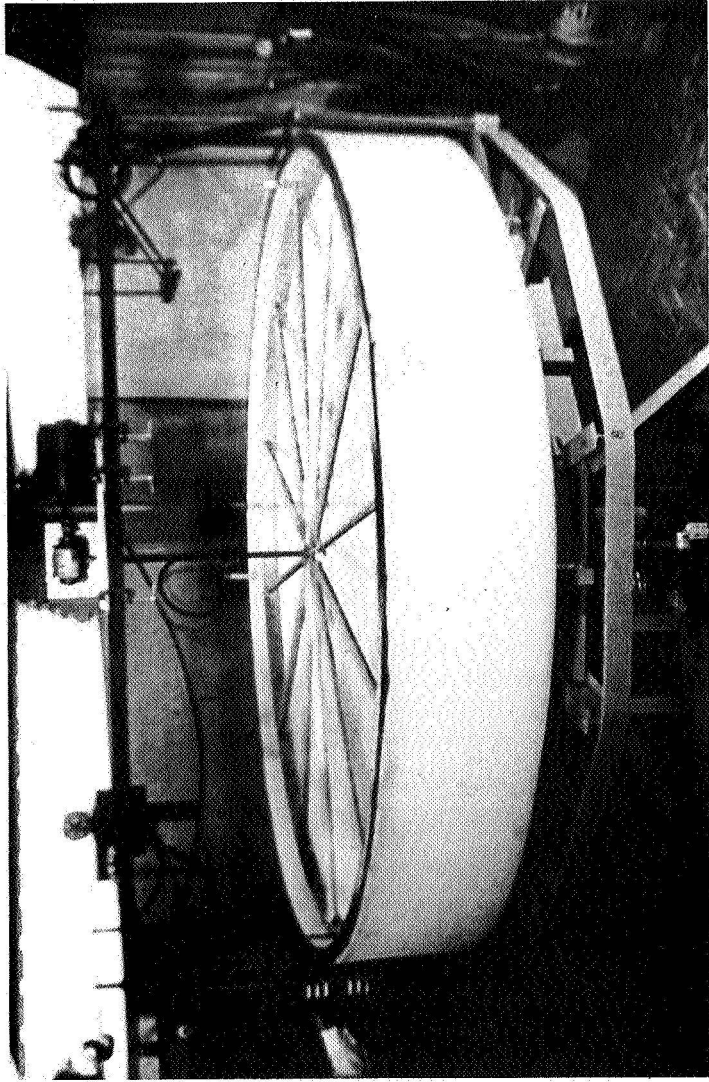


Figure 7

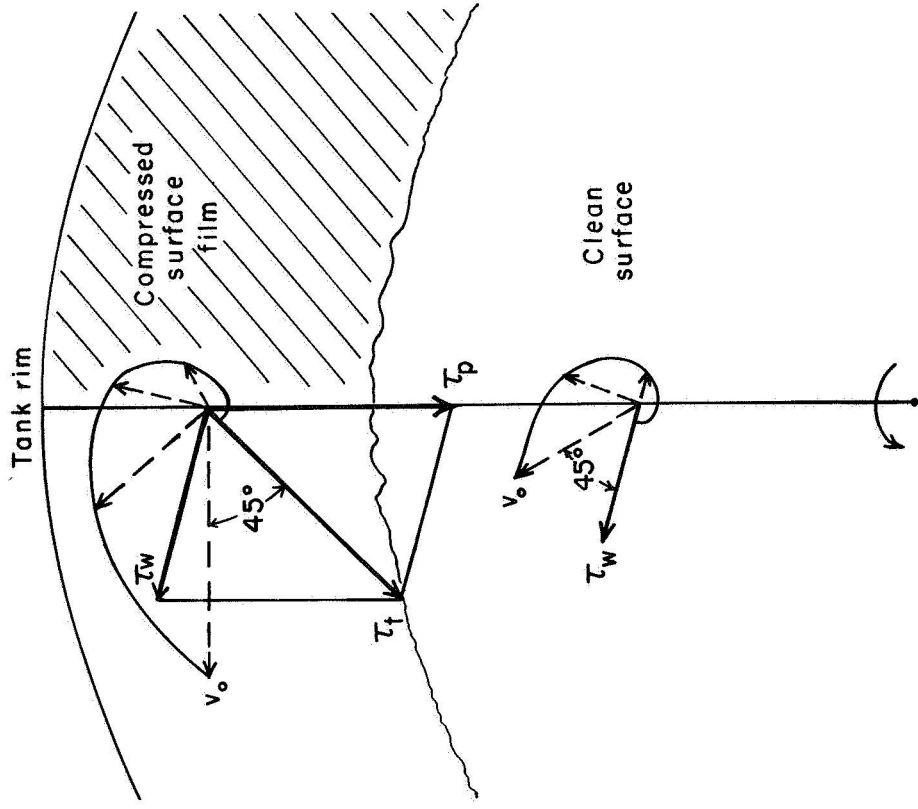


Figure 8

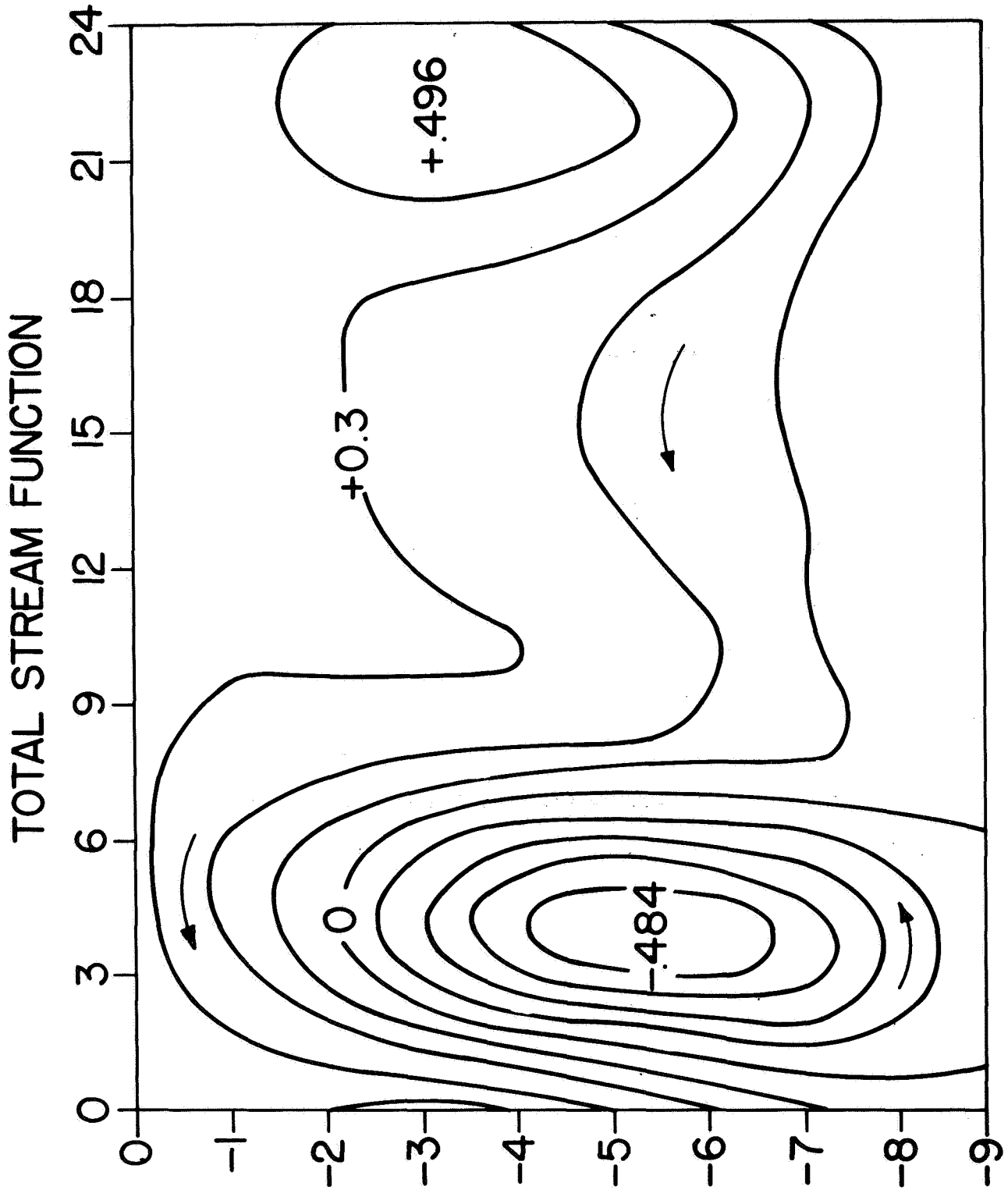


Figure 9a

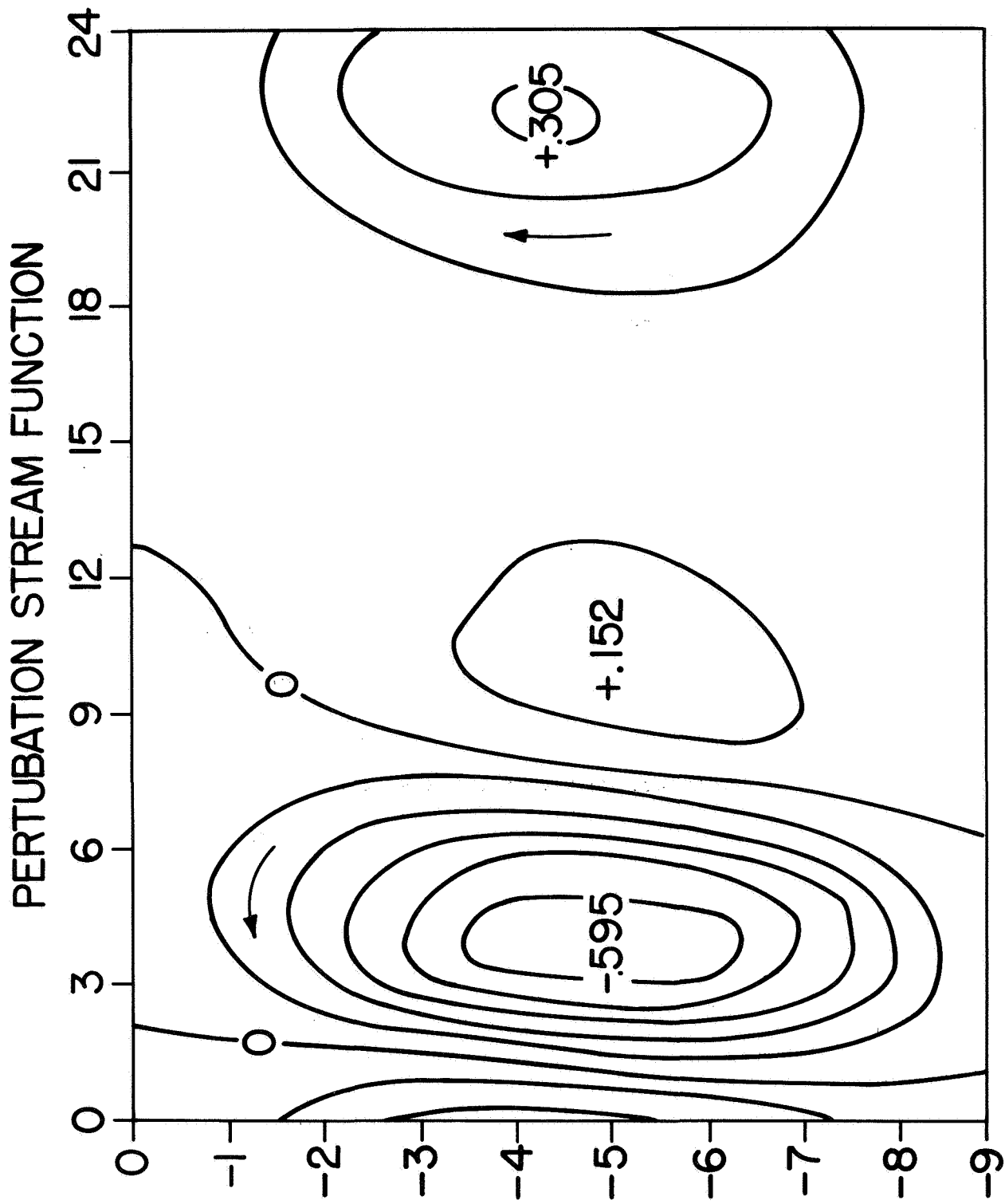


Figure 9b

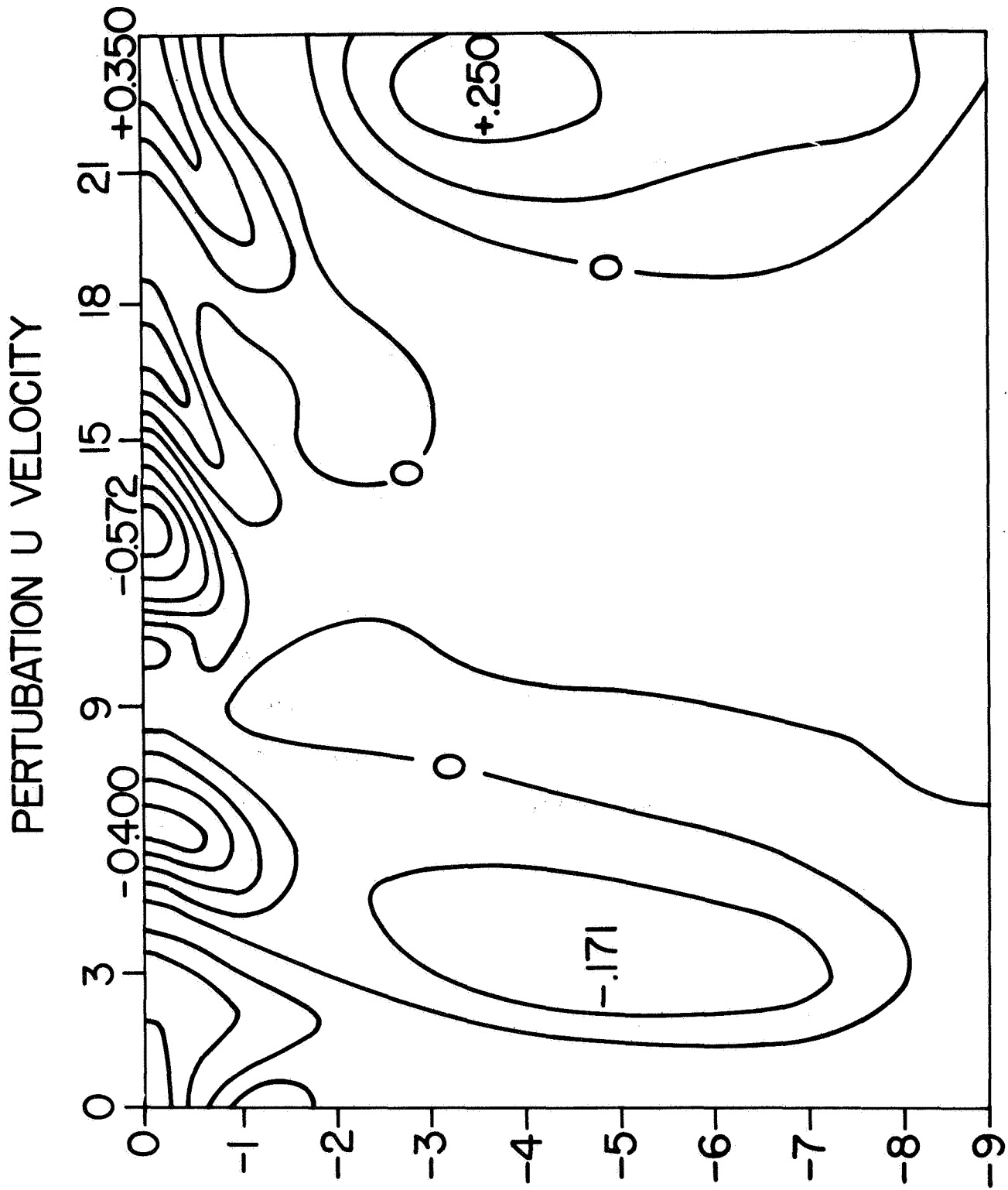


Figure 9c

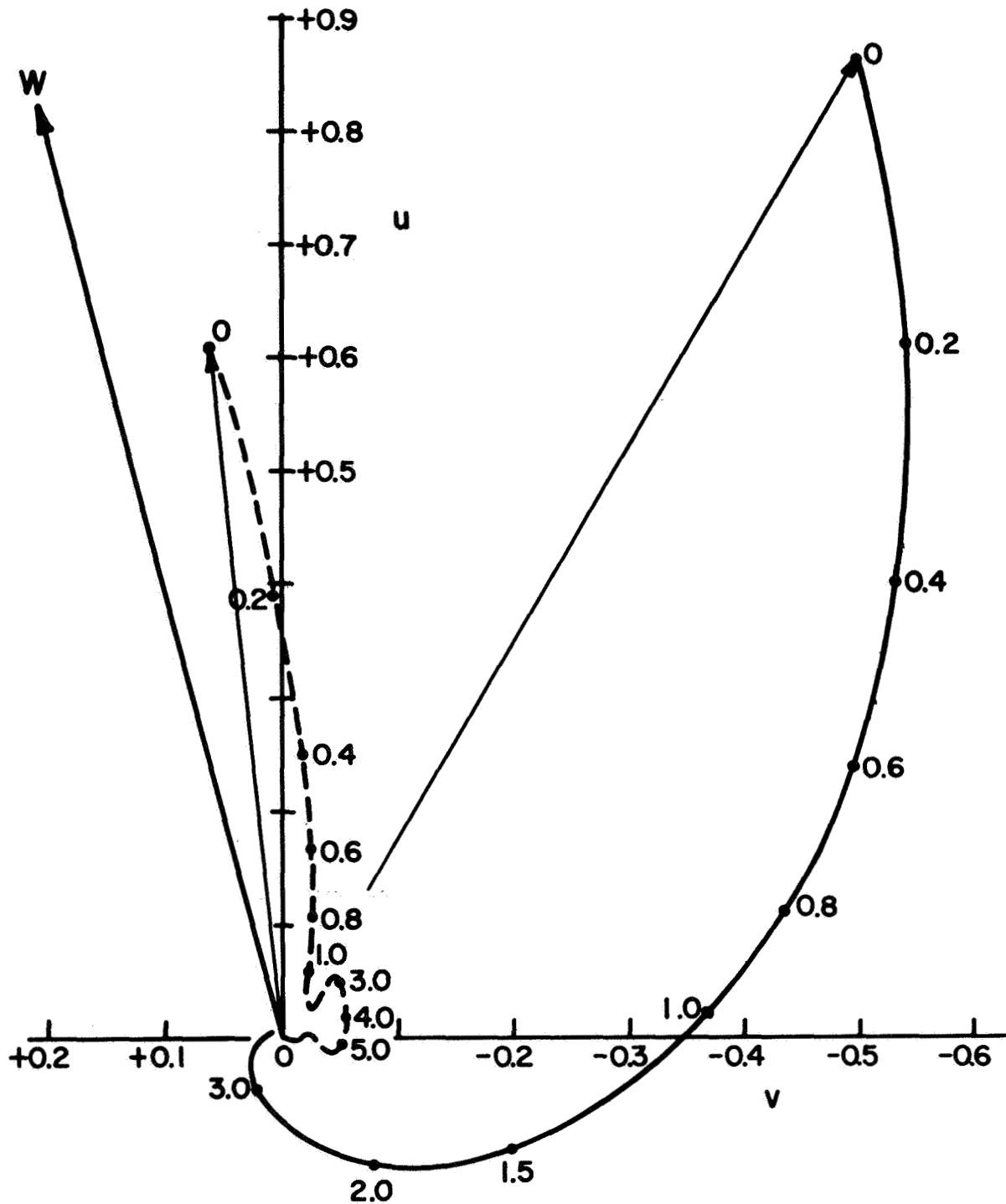


Figure 10

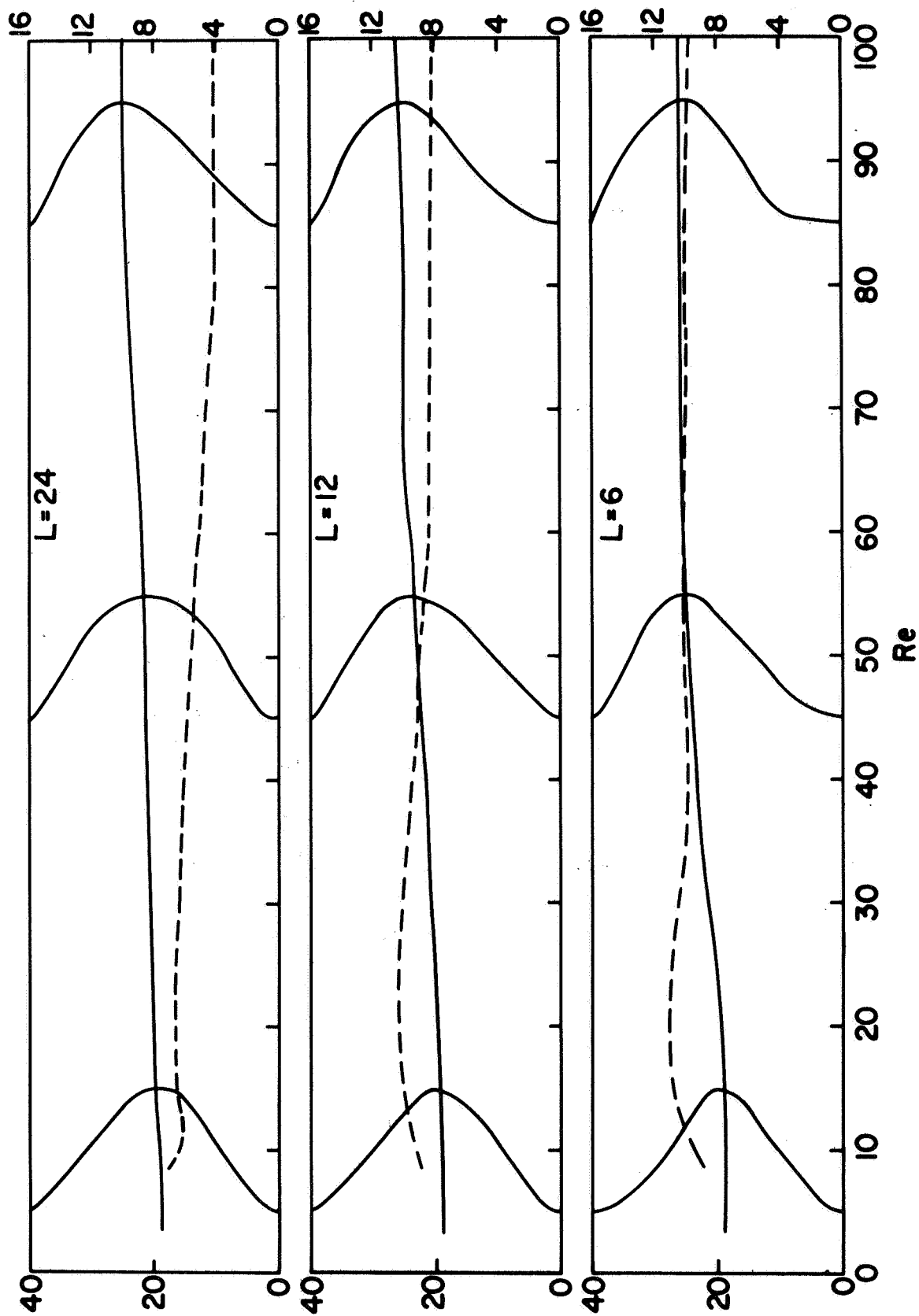


Figure 11

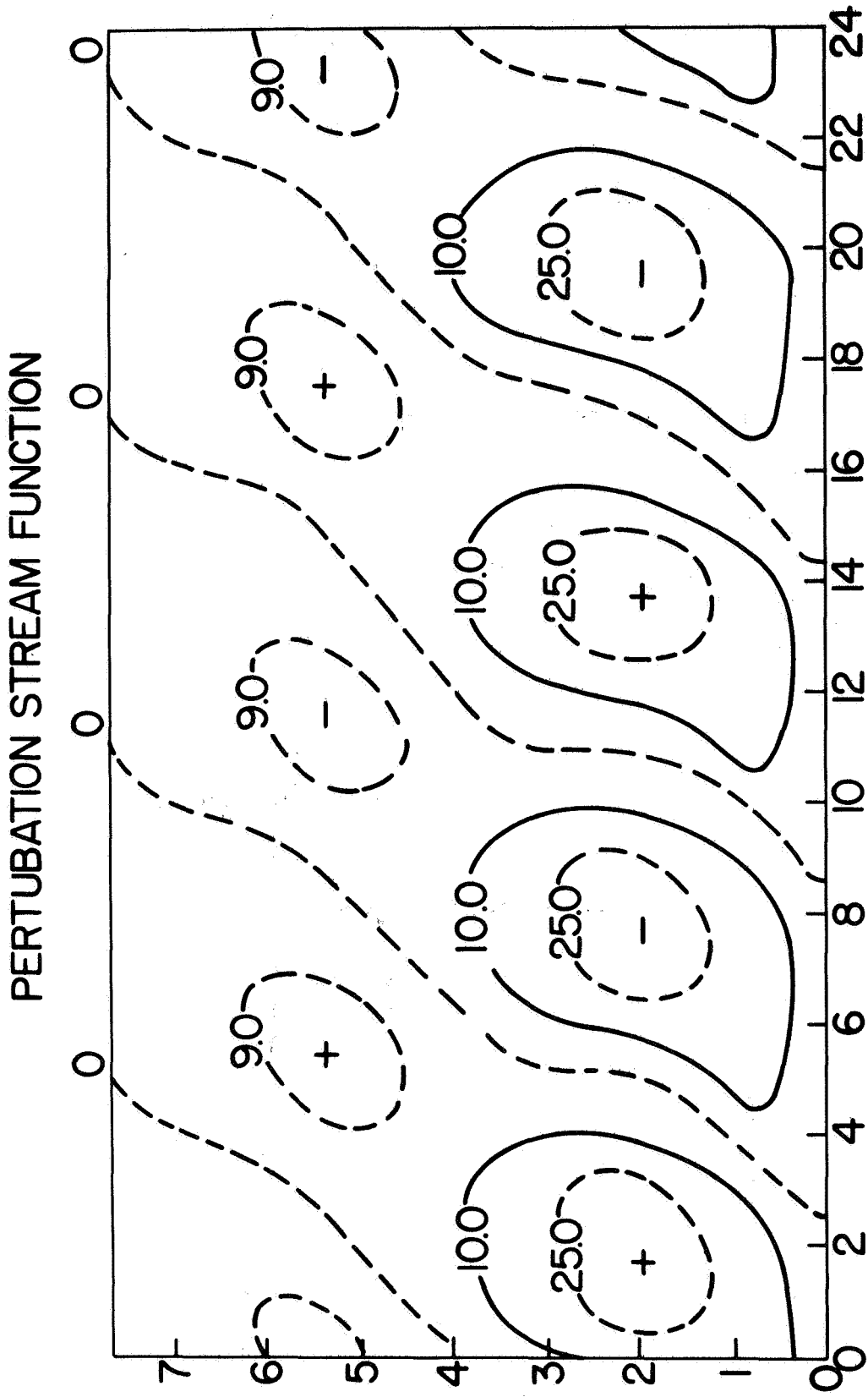


Figure 12a



PERTUBATION STREAM FUNCTION

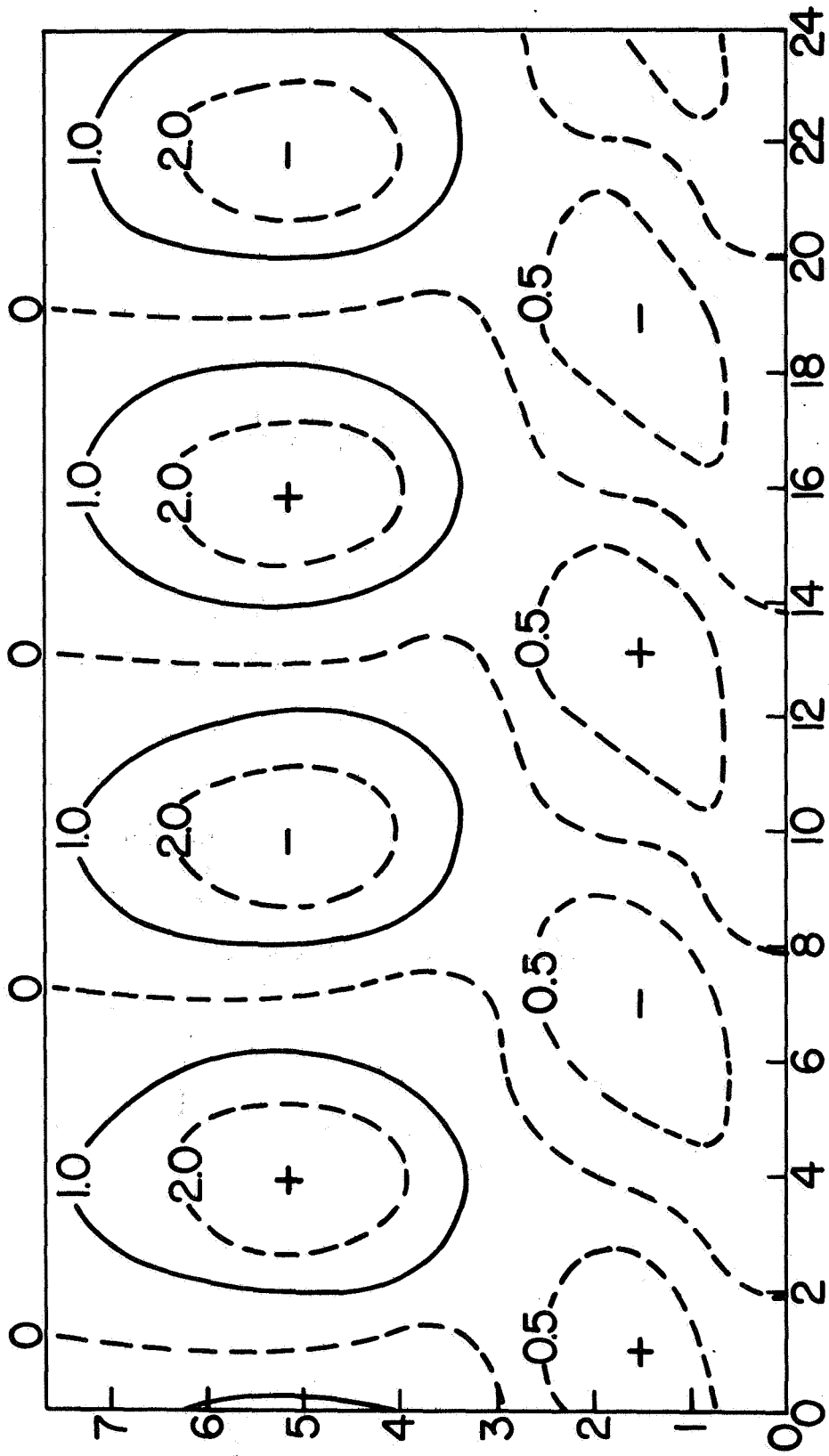
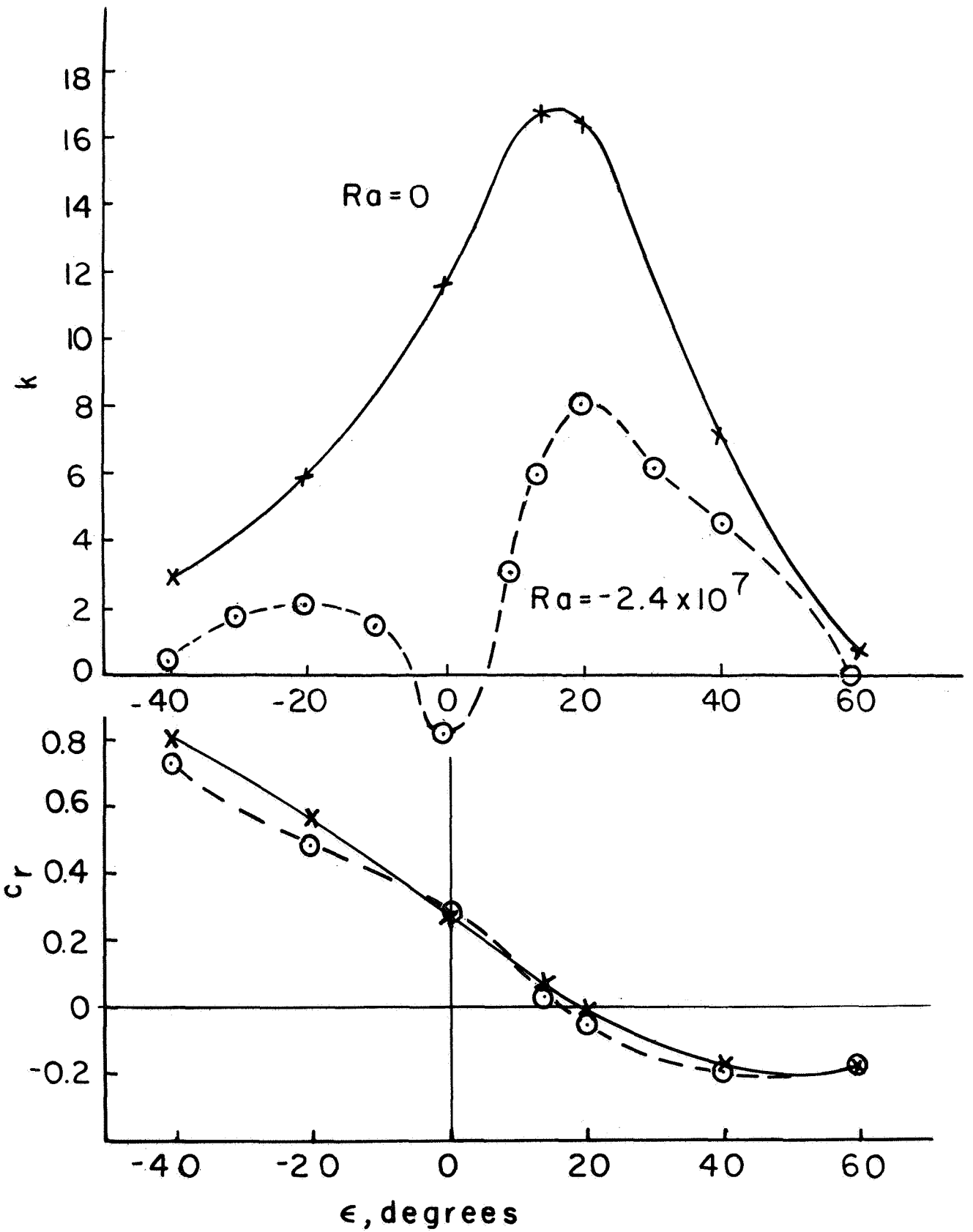


Figure 12b



**Figure 13**